Earth Planet. Sci. Lett. 676 (2026) 119782

Contents lists available at ScienceDirect

Earth and Planetary Science Letters

journal homepage: www.elsevier.com/locate/epsl

Changing volatile emissions and sources along the Ethiopian Rift

Abate A. Melaku [a,b,*], Gemechu B. Teferi [b], Takele Mihretie [c], Snorri Gudbrandsson [d], Yared Sinetebeb [e], Peter H. Barry [f], Tobias P. Fischer [g], Finlay M. Stuart [h], Ugur Balci [h], Sæmundur A. Halldórsson [i], Chris J. Ballentine [j], Darren J. Hillegonds [j], Emma L. Chambers [k], Derek Keir [l,m], Richard Bates [a], William Hutchison [a]

[a] School of Earth and Environmental Sciences, University of St Andrews, St Andrews, UK
[b] School of Earth and Planetary Sciences, Addis Ababa University, Addis Ababa, Ethiopia
[c] Department of Geology, Debre Berhan University, Debre Berhan, Ethiopia
[d] Reykjavik Geothermal Ltd., Reykjavik, Iceland
[e] Ethiopian Electric Power, Aluto Geothermal Expansion Project, Ethiopia
[f] Woods Hole Oceanographic Institution, Woods Hole, Ma, USA
[g] Department of Earth Science, University of California Santa Barbara (UCSB), California, USA
[h] Scottish Universities Environmental Research Centre (SUERC), East Kilbride, UK
[i] Nordvulk, Institute of Earth Sciences, University of Iceland, Reykjavik, Iceland
[j] Department of Earth Sciences, University of Oxford, Oxford, UK
[k] Dublin Institute for Advanced Studies, Dublin, Ireland
[l] School of Ocean and Earth Science, University of Southampton, Southampton, UK
[m] Dipartimento di Scienze della Terra, Università degli Studi di Firenze, Florence, Italy

ARTICLE INFO

Editor: Dr C. M. Petrone

Keywords:
CO_2 emissions
Mantle plume
Ethiopia
Rift
Magmatism
He isotopes

ABSTRACT

Rift volcanoes are sites of intense volatile emissions. However, major uncertainties remain about the magnitude of rift volatile fluxes, particularly for greenhouse gases (e.g. CO_2) and whether along-rift variations in degassing relate to changing mantle sources and/or rifting processes (i.e. melt production and lithospheric thinning). Here, we investigate CO_2 flux and gas isotopes in Ethiopia; a mature, plume-influenced continental rift. We focus on one of the largest caldera volcanoes, Bora-Baricha-Tulu Moye (BBTM), which is situated in a region of high mantle melt production in the Central Main Ethiopian rift (~500 km south-west the putative plume head). BBTM gases are characterized by plume-like $^3He/^4He$ values up to 17 R_a (the highest ever observed in Ethiopian Rift fumaroles) and we calculate total magmatic CO_2 flux of 757–901 t d^{-1} (making BBTM the largest volcanic CO_2 emitter in the Ethiopian Rift). Using our CO_2 flux measurements, we estimate total CO_2 emissions from Ethiopia's volcanic systems to be 2500–9200 kt yr^{-1} and reveal important along-rift variation in CO_2 flux. High CO_2 flux sectors are found in Central Afar, as well as the Northern and Central Main Ethiopian Rift. These sectors are all regions of high partial melt content (evidenced by low seismic velocity in the underlying mantle) and also show the greatest $^3He/^4He$ values (>14 R_a). Cooccurrence of high mantle melt production, elevated CO_2 emissions and high $^3He/^4He$ demonstrates that in mature continental rifts carbon emissions and plume volatile contributions are particularly elevated in regions of greatest lithospheric thinning and mantle melting.

1. Introduction

Continental rifts are a key component of Earth's deep volatile cycle (e.g. Lee et al., 2016; Brune et al., 2017). Much recent research has focused on carbon emissions in the East African Rift System (EARS, the largest continental rift on Earth), and various authors have measured CO_2 flux using satellite (Sawyer et al., 2008) and ground-based methods (e.g. Hutchison et al., 2015, 2023). Extrapolation of these data to the eastern sector of the EARS indicate CO_2 fluxes on the order of 10,000–100,000 kt yr^{-1} (Lee et al., 2016; Hunt et al., 2017), which suggest deep C emitted from continental rifting could initiate climate change over geological-timescales (Brune et al., 2017). However, these extrapolations are based on a few case studies of individual volcanoes and faulted areas, and there remains limited understanding of how CO_2

* Corresponding author at. School of Earth & Environmental Sciences, University of St Andrews, UK.
E-mail address: aam27@st-andrews.ac.uk (A.A. Melaku).

https://doi.org/10.1016/j.epsl.2025.119782
Received 20 November 2024; Received in revised form 1 December 2025; Accepted 7 December 2025
Available online 18 December 2025

emissions vary spatially and, crucially, between different sectors (Muirhead et al., 2020).

CO_2 emissions within a given rift segment depend on the C content of the lithospheric and asthenospheric mantle sources, the melt production rates from these sources, and the availability and permeability of degassing pathways (Hunt et al., 2017). Recent studies have suggested that lithospheric mantle sources could be a significant store of deep C (Foley and Fischer, 2017) and that during continental rifting large quantities are displaced and remobilized (Muirhead et al., 2020). In East Africa the role of the mantle source in controlling volatiles emissions is complicated by the presence of one or more upwelling mantle plumes (Pik et al., 2006; Halldórsson et al., 2014). While accepted that the region is underlain by a large low-velocity anomaly rooted in the core-mantle boundary (Ritsema et al., 1999), its presence and architecture in the upper mantle remain controversial (Chang et al., 2020; Boyce et al., 2023). Plume materials continue to provide heat (Rooney, et al., 2012a), primordial volatiles (Halldórsson et al., 2014; Balci et al., 2024) and potentially recycled crustal volatiles (Halldórsson et al., 2022) to rift magmas. However, it remains unclear how these sources vary spatially and whether CO_2 emissions are elevated in more plume influenced regions.

The Ethiopian Rift offers an opportunity to explore the links between CO_2 degassing, changing mantle sources and processes (i.e. melt production and lithospheric thinning). It represents a variably plume-influenced region (Halldórsson et al., 2014), that captures the transition from continental rifting to incipient seafloor spreading (Ebinger, 2005; Corti, 2009). Key evidence for a plume contribution comes from noble gas isotopes, particularly helium ($^3He/^4He$) in volcanic rocks and gas emissions, which fingerprint different mantle and crustal sources (Graham, 2002). Helium isotopes, expressed as air-corrected $^3He/^4He$ (R_c/R_a), show elevated values in northern Ethiopia (Afar and Gulf of Tadjoura) as well as the Central Main Ethiopian Rift (CMER) where erupted basalts display $^3He/^4He$ of 10.0–16.9 R_c/R_a indicative of deep mantle sources (e.g. Scarsi and Craig, 1996; Marty et al., 1993; Balci et al., 2024). In southern Ethiopia recent volcanics and geothermal gases have low He isotope ratios (4.0–7.5 R_c/R_a, Halldórsson et al., 2014; Hutchison et al., 2023), suggesting greater radiogenic ^4He contributions from crustal sources. These are consistent with other geochemical tracers (e.g. Sr, Nb, Pb-isotopes) which support a large-scale southward decrease in plume input (Rooney et al., 2012b) and smaller scale

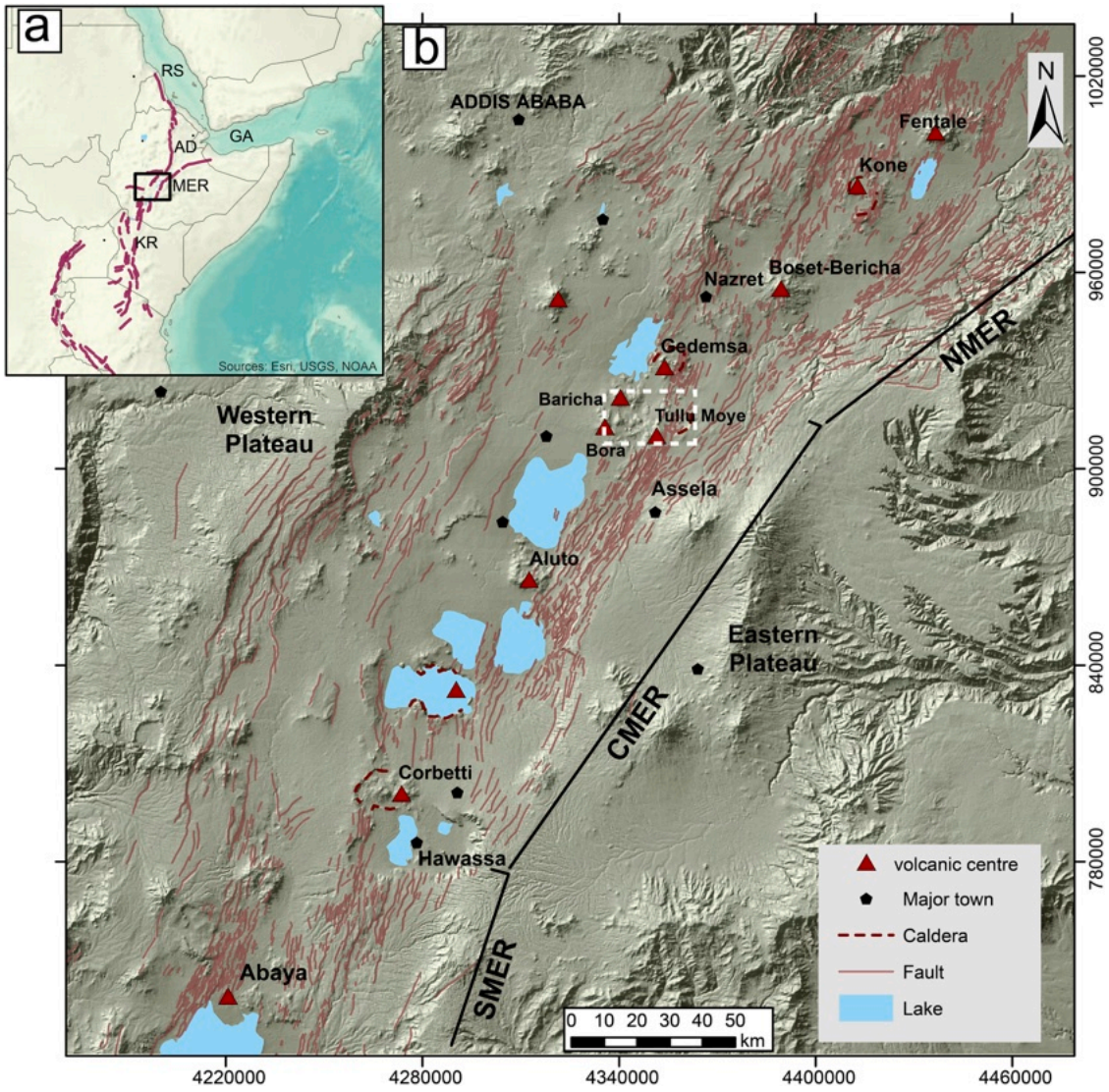

Fig. 1. (a) Overview map of the East African Rift System (EARS) and (b) the Main Ethiopian Rift (MER) showing key volcanic and tectonic features. The northernmost point of the EARS marks the Afar triple junction where the Afar Depression (AD), Red Sea (RS) and Gulf of Aden (GA) rifts meet (red lines outline boundaries of the rifts). The MER is sub-divided into southern, central, and northern sectors, SMER,CMER and NMER, respectively. Faults are after Agostini et al. (2011) and the location of Bora-Baricha-Tulu Moye (BBTM) is indicated by the white dashed rectangle.

chemical heterogeneity along-rift (Watts et al., 2025).

Interestingly, geophysical data also reveal important along-rift variations in mantle melting and magmatism. For example, seismic tomography shows that upper mantle melt production is segmented with the lowest seismic velocities and highest volumes of partial melt beneath central Afar, the NMER and CMER (Gallacher et al., 2016; Chambers et al., 2022). These segmented melt zones, spaced ~100–300 km apart, are comparable to those observed in more mature oceanic rifts such as the Gulf of California (Wang et al. 2009).

To date, only a handful of CO_2 studies have been conducted in the Ethiopian Rift (Hutchison et al., 2015, 2023; Hunt et al., 2017). These highlight the important role that volcanic and tectonic structures play in controlling gas emissions and emphasise that degassing through rift faults is highly spatially variable. Hunt et al. (2017) showed that CO_2 emissions are concentrated at discrete volcanic systems which require detailed structural mapping and CO_2 flux surveys to quantify emissions. Despite this, no study has investigated CO_2 flux at the largest caldera volcanoes in high magma flux regions, and it is unclear whether CO_2 flux varies along-rift and whether this is influenced by changing mantle sources (lithospheric, asthenospheric or plume lithologies) and/or mantle melt production.

Here we focus on Bora-Baricha-Tulu Moye (BBTM, Fig. 1), one of the most melt-rich magmatic systems in the CMER (Dambly et al., 2023). We report new soil CO_2 flux and isotopic (C and He) analyses of fumarole gases. We use this to improve estimates of CO_2 emissions along the different sectors of the Ethiopian Rift and explore the relationship between CO_2 emissions, mantle sources and melt production using a large-scale compilation of He-isotope and seismic tomography data from across the rift.

2. Geological background

2.1. The Ethiopian Rift

The Ethiopian Rift is a zone of continental extension between the Nubian, Somalian and Arabian plates (Corti, 2009; Fig. 1a). At its northernmost extension in Afar, rifting is most advanced and transitioning into incipient seafloor spreading (Ebinger, 2005; Corti, 2009). In central and southern Ethiopia, the MER connects Afar to the Turkana Depression and Kenyan Rift (Fig. 1). The MER is divided into Northern, Central and Southern sectors (NMER, CMER, SMER, respectively, Fig. 1, Hayward and Ebinger, 1996). Based on the rift architecture and lithospheric thickness it is generally accepted that rift maturity increases northwards (Agostini et al., 2011). The rift sectors are characterized by two distinct fault systems: 1) border faults and 2) axial faults, referred to as Wonji Faults (Boccaletti et al., 1998). In the CMER, the location of our survey, border faults are defined by NE-trending with large vertical throws (>500 m) (Agostini et al., 2011; Corti et al., 2018). The Wonji Fault Belt (WFB) is represented by a high density of NNE-trending right-stepping en-echelon faults (Boccaletti et al., 1998), with throws of <100 m and fault slip rates of 2–4 mm yr^{-1} (Siegburg et al. 2020).

2.2. Bora-Baricha-Tulu Moye (BBTM) volcanic complex

BBTM is in the northern part of the CMER (Fig. 1) and comprises three major silicic edifices (Bora, Baricha, Tulu Moye) and several smaller centres (e.g., Werdi and Oda, Fig. 2a; Tadesse et al., 2022). It is thought to represent overlapping calderas (Tadesse et al., 2023a; Fig. 2) with the youngest caldera-forming eruption dated to 107.7 ± 8.8 ka (Tadesse et al., 2022).

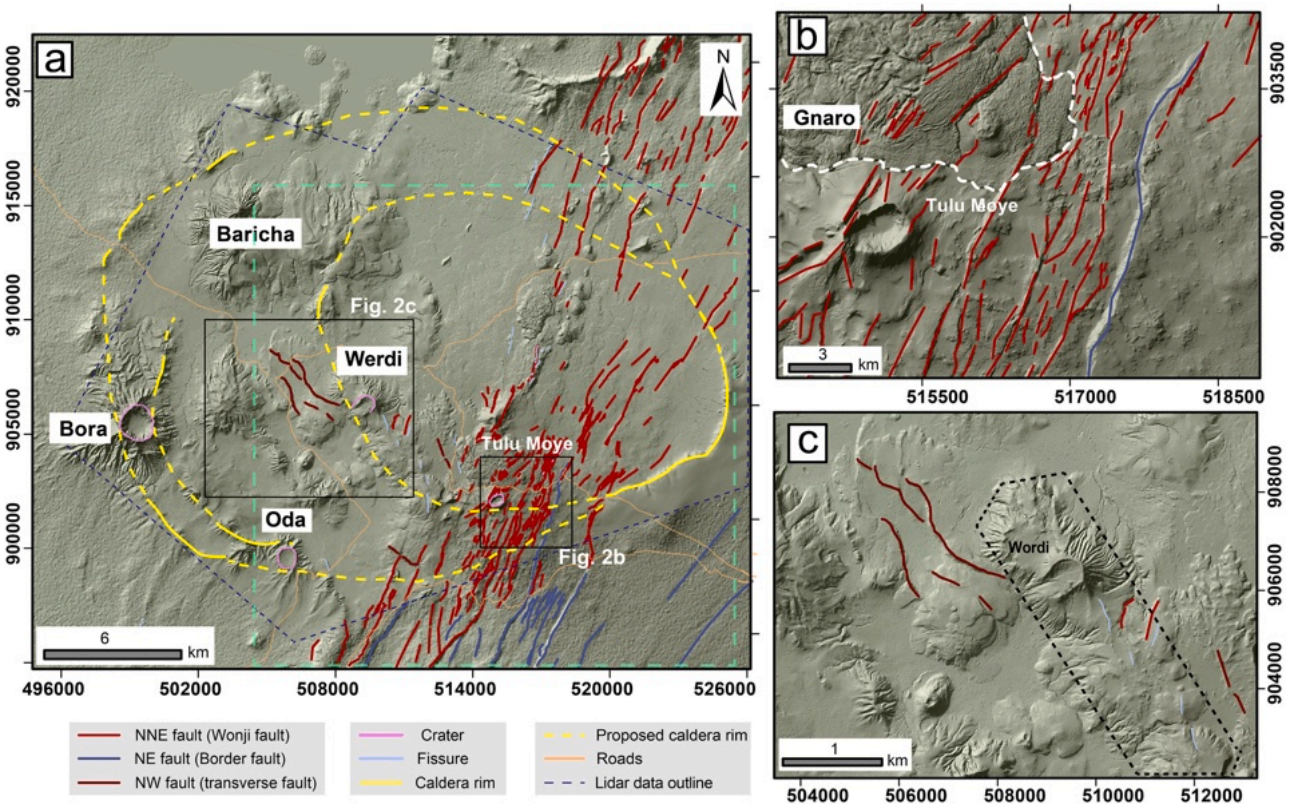

Fig. 2. (a) Shaded relief map of the Bore-Baricha-Tulu Moye (BBTM) volcanic complex showing faults (with colour based on orientation and classification). Craters, visible caldera rims (solid yellow line), and proposed calderas (dashed yellow line, after Tadesse et al. 2023). The LiDAR footprint is shown by the dashed blue line and the outline of Fig. 3 by the dashed green line. Black boxes correspond to inset maps b and c. (b) shows NNE Wonji faults concentrated on the eastern side of the complex and the dashed white line shows the Gnaro lava dome (c) shows NW trending faults, and the dashed black lines indicates the NW trending pumice dome and basaltic fissures.

Geophysical studies show that BBTM is seismically active and deforming and have linked this to hydrothermal circulation above an inflating magma reservoir (Greenfield et al., 2019a, 2019b). Magnetotelluric imaging supports magma reservoirs at ~5 km and >8 km depth (Samrock et al., 2018; 2021). The most recent activity at BBTM is focused along a NE-SW cluster of vents and includes obsidian coulees (Gnaro, and Giano, Fig. 2), basaltic flows and scoria cones (e.g. Tulu Moye pyroclastic cone, Fig. 2b) along a faulted ridge: the Salen range (Tadesse et al., 2022). Fumaroles, hot grounds and surface alteration have also been identified across the complex (Benvenuti et al., 2023; Fig. 3a).

BBTM is cut by a dense network of seismically active faults and the majority of these belong to the WFB (Keir et al., 2006; Greenfield et al., 2019b). These faults are dilatational, as confirmed by field analysis (Acocella et al., 2003), and the focal mechanisms of the earthquakes mainly show normal slip (Greenfield et al., 2019a). Magnetotellurics and geological mapping suggest that melt migrates and accumulates along faulted zones and that these faults help guide magma to the surface (Samrock et al., 2018; Tadesse, et al., 2023b).

3. Methods

3.1. Remote sensing and mapping

Maps of volcanic features and tectonic structures at Tulu Moye and across the Ethiopian Rift were made using Google Earth imagery as well as digital elevation models (DEMs) from satellite (12.5 m resolution ALOS PALSAR) and airborne (2 m resolution LiDAR) data. A detailed description of our vent density and structural mapping is provided in the Supplementary material.

3.2. Soil CO_2 measurements

Soil CO_2 measurements were conducted in several campaigns between June 2015 and May 2022 (detailed in the Supplementary Information). A 50–100 m measurement site spacing was used when transecting major fault structures and a 20 × 50 m sampling grid for detailed surveys north and south of the Gnaro lava dome (Fig. 3b). Gaussian Geostatistical Simulation (GGS, Cardellini et al., 2003) was used to produce maps of CO_2 flux from dense grids. To calculate the CO_2 flux for the complex we divided the study area into regions of similar volcano-tectonic degassing and carried out transects across these. We fit each transect with a stepped line and used the area under the curve to calculate CO_2 flux. We then calculate the flux of these regions using their width (i.e. distance orthogonal to the transect line) and obtain a total CO_2 flux for the complex by summing these regions (detailed in Section 4.4).

Gas samples were collected in pre-evacuated vials in 2016 (n = 7) and 2022 (n = 64). The 2016 samples were from fumaroles and were analysed for CO_2 -$\delta^{13}C$ at the Department of Earth and Planetary Sciences at the University of New Mexico. The analytical setup is the same as described in Hutchison et al. (2023). The 2022 samples were collected from the accumulation chamber via a syringe with a shut off valve (Chiodini et al. 2008). CO_2-$\delta^{13}C$ analysis was performed at the Iso-Analytical laboratory at Crewe, UK using a GC Isotope Ratio Mass Spectroscopy (GC-IRMS). Gases were flushed through a packed GC column, and the resulting chromatographic peak was directed into a Europa Scientific Hydra 20–20 IRMS, where the isotopomers at m/z 44, 45, and 46 for CO_2 were measured. These were used to determine $\delta^{13}C$, reported as per mil values (‰) relative to PDB (Pee Dee Belemnite) using an internal standard. All $\delta^{13}C$ samples are characterized by a standard error of ±0.2 ‰.

3.3. Fumarole sampling for He isotope analysis

Samples for He isotope analysis were collected from high-temperature fumaroles using an inverted funnel (e.g., Barry et al., 2022). The sampling line was flushed for 1–2 h, and the gases were captured in 3/8-inch refrigeration-grade copper tubes by sealing the ends with stainless-steel clamps.

We collected samples in 2019 (PB-samples in Supplementary Table S3) and revisited 3 sites in 2022 (TMF-samples). He isotope analysis of four samples from 2022 was conducted at Scottish Universities Environmental Research Centre (SUERC). Each sample (~10 cm^3 gas) was expanded to a titanium sublimation pump at 900 °C and a series of SAES GP50 ZrAl getters at 250 °C operating under ultra-high vacuum (Gyore et al., 2015). He isotopic composition was determined using a MAP 215–50 mass spectrometer relative to the HESJ standard. Analysis of the 2019 samples was conducted at the University of Oxford in an identical analytical procedure as described by Hutchison et al. (2023). These data are supplemented with He isotopes from two fumarole samples (ETH-56 and ETH-59) from the same region collected in 2012 and analysed at Scripps Institution of Oceanography following methods identical to those described by Halldórsson et al. (2013).

4. Results

4.1. Structural analysis

Key volcanic and tectonic structures of BBTM are shown in Fig. 2. We identify three main fault sets with NNE-SSW, NE-SW, and NW-SE trends. NNE-SSW faults are the most dominant and appear as sub-vertical (60–85°) closely spaced scissor-type normal faults with lengths of 10′s m to ~6 km and vertical displacements <100 m (Fig. 2b). A dense network of these faults crosses through the east of Tulu Moye, and these closely match the trend and architecture of the <2 Ma WFB (Boccaletti et al., 1998). NE-SW trending faults are mainly exposed in the south-eastern part of the complex. Compared to the NNE-SSW faults, they are longer (>2000 m), with greater vertical offset (up to 250 m) and dips of 70–85° (Supplementary Figures) and are more akin to rift border faults (Agostini et al., 2011). NW-SE (rift transverse) faults occur west of Werdi where they range from 20 to 2000 m long (Fig. 2c) and have vertical offsets of ≤70 m with ≤65° dip. Fumaroles, hot grounds and hydrothermal alteration (Fig. 3a) also occur along this NW-SE trend, where pumice deposits and basaltic fissures form an elongate ~4 km long dome (black-dashed outline in Fig. 2c).

Remnant calderas are identified across the complex. The most obvious is the ~10 km long, ~300 m high rim on the north-eastern part of the complex (Fig. 3). Additional inward-dipping caldera rims are identified at Oda and Bora (Fig. 2), and we outline other potential calderas after Tadesse et al. (2022).

4.2. Soil CO_2 flux dataset

Fig. 3b shows soil CO_2 flux values at BBTM. These range from 0.11 to 1107 g m^{-2} d^{-1}. Highest flux values are adjacent to thermal manifestations and follow major faults and fractures south and north of the Gnaro obsidian dome (along the Salen range and Werdi regions, Fig. 3). Measurements focussing on Wonji faults (SE of Tulu Moye cone) and the caldera escarpment east of the study area generally show lower flux (~10 g m^{-2} d^{-1}). To constrain a non-volcanic background flux value, we measured CO_2 flux in various soils 5–10 km east of Tulu Moye. These range from 0.48 to 8.60 g m^{-2} d^{-1}. The upper value was taken as a maximum background flux and used to define regions of anomalous magmatic-hydrothermal (i.e. those >8.60 g m^{-2} d^{-1}).

4.3. Soil CO_2 flux profiles

CO_2 flux transects are shown in Fig. 4. A-A' shows a west-to-east transect crossing the major Wonji faults to SW of the Gnaro obsidian lava dome (Fig. 3b). On the east of the profile (between 1 and 2.5 km) high CO_2 fluxes are associated with normal fault scraps (maximum

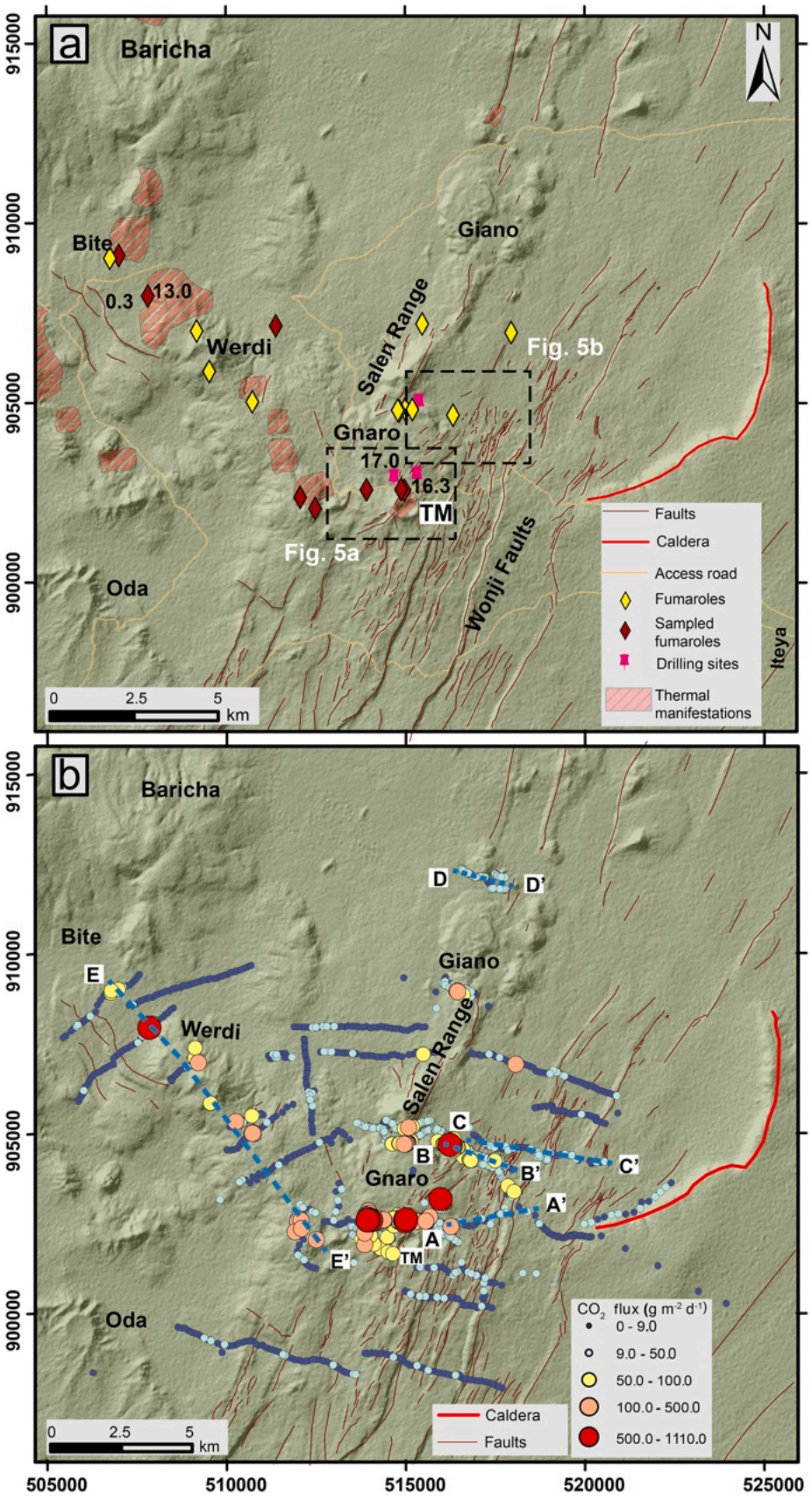

(caption on next page)

Fig. 3. a) Locations of thermal manifestations (hot and altered grounds) and (fumaroles) at Bora-Baricha-Tulu Moye (BBTM). Numbers give the air corrected $^{3}He/^{4}He$ values from the corresponding fumarole. b) discrete soil CO_2 measurements (Supplementary Table S1) with symbol size and colour tied the magnitude of the flux (see legend). The blue dashed lines represent CO_2 degassing transects across the faults (labelled A–E and shown in Fig. 4). High CO_2 flux is concentrated along the faults, fumaroles and altered grounds. Our range and choice of background value compare with previous measurements in the CMER (e.g., 0.5–6.0 g m^{-2} d^{-1}, W. Hutchison et al., 2015).

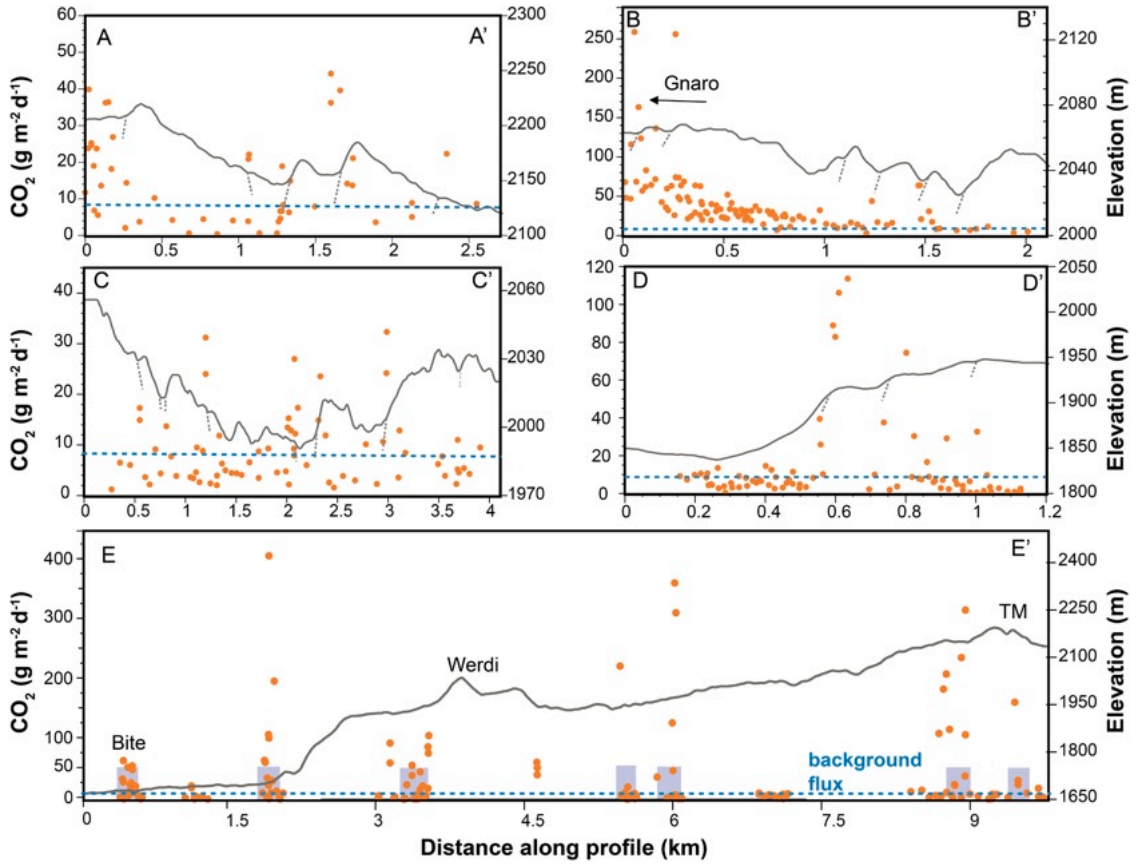

Fig. 4. CO_2 degassing transects (represented by the blue dash lines in Fig. 3b) across the Bora-Baricha_Tulu Moye (BBTM) complex . Faults are represented by grey dashed lines, and the profiles show a 10x vertical exaggeration. The blue dashed line indicates the upper limit of the background CO_2 flux (8.6 g m^{-2} d^{-1}, Section 4.2). The grey vertical rectangles in transect EE' represent the main thermal manifestations distributed along the Werdi rift transverse structures (Fig. 3a, Section 4.3).

values of 44 g m^{-2} d^{-1} in the hanging wall). Between 0.5–1 km, where major faults are absent, the CO_2 flux is below background. On the approach to Gnaro lava dome (at ~0 km), the maximum flux values increase, yet there is no obvious structural feature at the surface. B-B' covers a ~2 km W-E transect from the densely faulted margin of the complex to the lava dome at Gnaro (Fig. 3b). In the east, normal fault scarps align with elevated CO_2. However, the most significant trend is increasing CO_2 from 1 to 0 km (west towards the Gnaro lava dome). The highest flux (260 g m^{-2} d^{-1}) is observed at the foot of the lava dome. This broad (~1 km) trend of increasing CO_2 is very different from the short (100 m) fault-controlled CO_2 anomalies seen elsewhere on BBTM. C—C' covers multiple Wonji faults north of B-B'. Highest CO_2 fluxes (32 g m^{-2} d^{-1}) coincide with the main fault zones at ~1 and ~3 km. Comparing CO_2 flux on faults covered in transects A-A', B-B' and C—C' (Fig. 3b), we find that CO_2 flux decreases northward, with the highest values occurring closest to Gnaro lava dome. D-D' crosses the northern tip of the Salen range and shows highest values (113 g m^{-2} d^{-1}) on faults at the axis of the range (at ~0.6 and ~0.8 km). Away from this CO_2 emissions mostly show background values. E-E' follows the NW-SE oriented dome of pumice and eruptive fissures with strong thermal manifestations from Bite to Tulu Moye (Fig. 3b). Elevated CO_2 fluxes occur across this area with peak values (>100 g m^{-2} d^{-1}) adjacent to thermal manifestations.

4.4. Soil CO_2 flux mapping and total flux

CO_2 maps from north and south Gnaro (generated using GGS, Section 3.2) show highest fluxes are associated with fumaroles (Fig. 5). Total CO_2 fluxes (mean ± 1σ) for south and north Gnaro are 33.1 ± 4.6 t d^{-1} and 12.5 ± 0.6 t d^{-1}, respectively.

Our application of the rectangular curve fitting technique to estimate total CO_2 emissions (Section 3.2) is shown in Fig. 6. We assign 12 degassing regions (A-L) across the surveyed area (94–103 km^2). A key uncertainty is the width of each degassing region (i.e. the distance orthogonal to the transect). We considered two scenarios. In the first case, we divide the area equally between two transects, i.e. extending the horizontal transect with an equal share of the area in between. In the second case, we reduce the extent of the high degassing regions (N- and S-Gnaro) by truncating the region at the furthest extent of the transect line (Fig. 6a). This reduces area of the high-degassing regions to 25 % of the first scenario (e.g., Fig. 6, profiles B-B', C—C', D-D') with the remaining area encompassed by the neighbouring degassing region. Given this range of scenarios (Supplementary Table S2), the total CO_2 emission for the ~100 km^2 is 283–409 t d^{-1}.

Our CO_2 survey and transect calculation cover about one-third of the entire ~340 km^2 area of BBTM (dashed yellow circle, Fig. 6a). To estimate flux from the whole complex we divide BBTM into western and

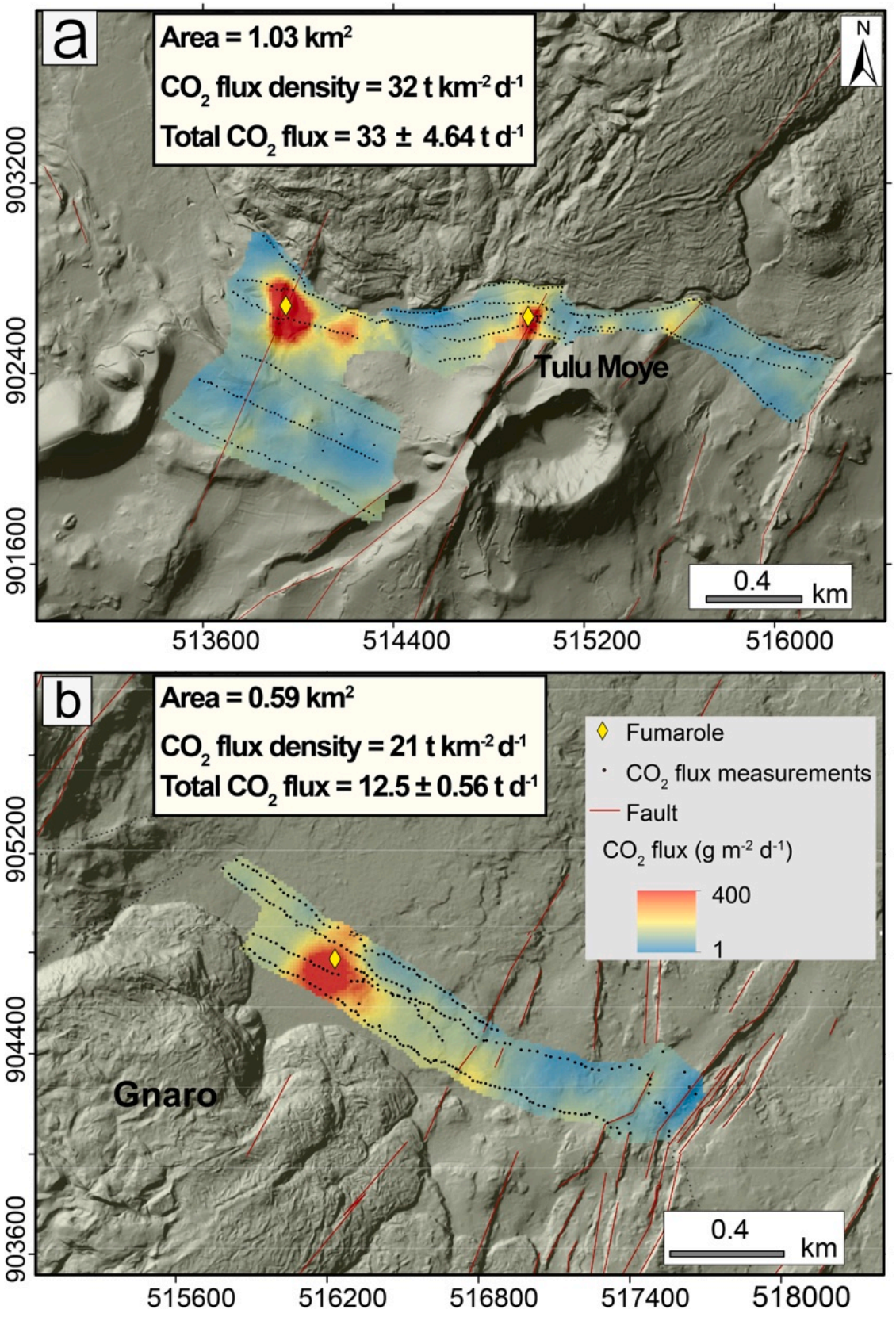

Fig. 5. CO_2 flux calculation for dense grids at south (a) and north (b) Gnaro. CO_2 flux maps were derived using a gaussian geostatistical simulation(GGS) approach (see Supplementary Information) and give the total CO_2 flux as the mean ± 1σ (of 100 simulations). Black points represent discrete gas flux measurements.

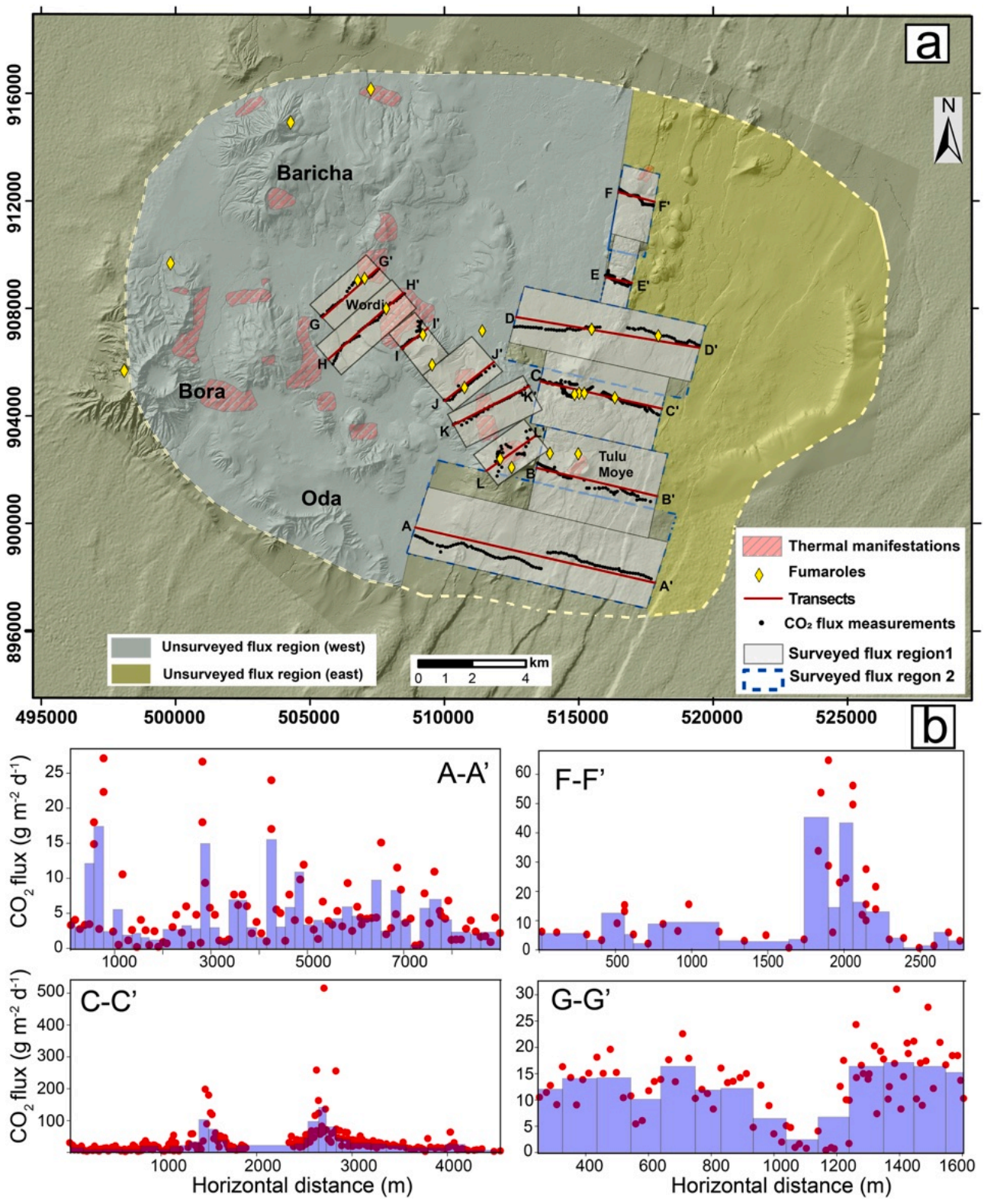

Fig. 6. CO_2 flux calculation using a rectangular fitting technique. a) shows the different polygons (areas) covered to estimate for the CO_2 emission. The red lines represent the flux profiles (transects) used to estimate the flux over the profile and the black points represent the discrete gas flux measurements. The yellow dashed line represents the total area of the Bora-Baricha-Tulu Moye (BBTM) complex, though we only consider the total flux over the surveyed regions and the unsurveyed western region (shaded blue). This value represents the end-member magmatic-hydrothermal degassing as we have removed a background contribution of 8.6 g m^{-2} d^{-1} (Section 4.2, Supplementary Table S2). Panels are rectangular curve fits for the profiles A-A', C—C', F-F' and G-G' as shown in Fig. 6a. The area under the curves represents the estimates of CO_2 flux per unit length along the profiles. The result is then be multiplied by the width of the polygons to estimate the flux over the area covered by each polygon shown in Fig. 6a (see Section 4.4 and 5.2 for full discussion of the method).

eastern regions (grey and yellow in Fig. 6) based on the occurrence of fumaroles, hydrothermal alteration and the tectonic and volcanic structures. The west region (grey in Fig. 6a) encompasses the volcanic edifices of Bora, Baricha and Oda. These areas are most like Werdi (GG' and HH' Fig. 6a) in terms of hydrothermal activity and fumarole intensity. Applying the CO_2 flux measured at Werdi (18 t d^{-1}) over this area gives a flux of 474–492 t d^{-1} for the western region of BBTM (237–246 km^2). Tadesse et al. (2022) suggested the BBTM system extends to the east of our surveyed area (yellow in Fig. 6a) and using the same scaling value from Werdi would give an additional CO_2 flux of 220 t d^{-1} (110 km^2). However, as there are no thermal manifestations (Fig. 6b) and our CO_2 measurements on the caldera escarpment east of Tulu Moye show low values (Fig. 3b) we consider the most realistic total CO_2 flux for BBTM to only include the transect areas and the western sector of BBTM. This yields a total CO_2 flux of 757–901 t d^{-1}.

4.5. Gas chemistry and C—He isotopic compositions

CO_2 concentration and $\delta^{13}C$ were determined for 64 soil gas samples (sampled from the accumulation chamber line) and 7 fumarole samples (Section 3.3). Soil gas samples show CO_2 contents of 452–6941 ppm and $\delta^{13}C$ of −3.79 to −13.03 ‰, while the direct fumarole samples show somewhat higher CO_2 contents of 1467–11,120 ppm and $\delta^{13}C$ of −1.1 to −5.1 ‰ (Fig. 7a,b). These data define a triangular array, interpreted as a mixture between air, biogenic and magmatic sources (Chiodini et al., 2008). Samples with highest CO_2 concentrations show $\delta^{13}C$ of −3 ‰, typical of magmatic CO_2 in the region (Hutchison et al., 2016).

$^3He/^4He$ ranges from 0.37 to 17.0 R_a (Fig. 7c). These data are corrected for atmospheric derived He (R_c/R_a) using measured $^4He/^{20}Ne$ following Hilton (1996) and are plotted against their X-vale (i.e. $^4He/^{20}Ne_{sample}/^4He/^{20}Ne_{air}$). X-values close to 1 mean the He is dominantly air-derived, while ≥10 is deeply sourced (i.e. either crustal and/or magmatic).

Eight samples were taken from five fumaroles (Fig. 3a). Of these, five show X-values close to 1. However, following air correction three of these show high $^3He/^4He$ up to 12 R_c/R_a (and we note there is no correlation between the X-value and the R_c/R_a value). X-values of the other three samples range from 289.6 to 1035.0 indicating limited air entrainment, and those with highest X-value show a significant plume contribution (13–17 R_c/R_a). It should be noted that using X-value to correct measured $^3He/^4He$ assumes that all ^{20}Ne derives from the atmosphere and yields a maximum estimate of the true $^3He/^4He$. This is a reasonable assumption particularly for the high (>100) X-value samples which show negligible difference between measured and corrected $^3He/^4He$ (Table S3).

5. Discussion

5.1. Structural controls on gas emissions

Fault mapping (Fig. 2) reveals BBTM is cut by NNE-SSW Wonji faults aligned parallel to the rift axis. CO_2 fluxes are significantly elevated along these structures (Fig. 4 AA', BB; CC') and particularly along the Salen range (from the Tulu Moye cone to Giano) where there is hydrothermal activity (Fig. 3a). Similar tectonic controls on CO_2 degassing have been identified in previous studies of the EARS (Lee et al., 2016; Hunt et al., 2017) and at other MER volcanoes (Hutchison et al., 2015, W. 2023).

Faults, thermal manifestations and anomalous CO_2 degassing also align NW-SE (Figs. 3b, 4EE'). Various authors have proposed that these NW-SE structures correspond to reactivated pre-rift faults (Korme et al., 2004; Benvenuti et al., 2023). This is supported by Tadesse et al. (2023a) who suggested that NW-SE faults at BBTM are crosscut by both the WFB and border faults, although given the large volumes of pyroclastic cover it is difficult to discern their length scale and whether they can be directly tied to transverse structures observed at the rift margins.

Highest CO_2 fluxes were measured close to the recent Gnaro obsidian coulee in the centre of the Salen range (Fig. 3b) in an area without obvious normal fault scarps. CO_2 transects from the Wonji faults towards the Salen range (Fig. 4BB') show increasing flux values over ~1 km which contrasts with the typically short length-scale (~10–100 m) CO_2 anomalies linked to faults. We hypothesize that this zone of steadily increasing CO_2 originates from a degassing source located beneath this lava flow at the centre of the Salen range. This may be an upwelling geothermal fluid or a shallow magmatic body, and since magnetotellurics supports a circular zone of partial melt body beneath Tulu Moye (Samrock et al., 2018), a magmatic intrusion seems most likely. The elevated CO_2 along the Salen range could also indicate a magmatic intrusion (i.e. a dyke, largely cooled and crystallised, with low melt fraction, undetectable by magnetotellurics) or simply higher rates of faulting along the Salen range and therefore greater permeability of the structure.

5.2. Deep C emissions from rift volcanic systems

Estimates of deep CO_2 emissions from continental rifting (10,000–100,000 kt yr^{-1}) suggest a globally significant flux (Lee et al., 2016; Foley and Fischer, 2017) that may initiate long-term climate change (Brune et al., 2017). In the Ethiopian Rift, Hunt et al. (2017) showed that C emissions are at the lower end of these estimates. They found that while rift faults are numerous, their CO_2 emissions were spatially heterogenous and generally low, and that greatest emissions were associated with areas of hydrothermal activity both on- and off volcanic edifices.

The current estimate for on-edifice degassing for the Ethiopian Rift is based on a single volcano (Aluto, Hunt et al. 2017). BBTM offers an opportunity to quantify emissions at the largest and most active volcanoes of the Ethiopian Rift. CO_2-$\delta^{13}C$ confirms that BBTM gases are an admixture of magmatic, biogenic and atmospheric C (Fig. 7a) and that samples with highest CO_2 contents (from sites of intense gas emission) display $\delta^{13}C$ between −2 and −6 ‰, overlapping both the canonical magmatic range −3 to −8 ‰ (Gerlach and Taylor, 1990) and the $\delta^{13}C$ of mantle xenoliths from Afar (−0.5 to −3.0 ‰, Halldórsson et al., 2022). To estimate CO_2 emissions for BBTM we calculated the flux along key transect lines (Fig. 6) then scaled these values up to account for the uncovered parts of the complex (Section 4.4). The scale-up considered the main edifices (i.e., Bora, Baricha and Oda) along with smaller volcanic vents as part of a single volcanic system. This is justified because magma geochemistry supports a single parental magma feeding the different centres (Tadesse et al., 2022, 2023b) and is further supported by magnetotelluric evidence for a single deep (likely mafic) magmatic reservoir beneath BBTM (from >8 km down to the mid-lower crust, Samrock et al., 2018). We also assessed the reliability of our curve fitting estimates by comparing our calculated CO_2 flux density to values obtained in areas of dense flux measurements (where it was possible to use GGS to create maps of CO_2 flux, Fig. 5). Flux density over south and north Gnaro from curve fitting (28 t $km^{-2}d^{-1}$ and 18 t $km^{-2}d^{-1}$, respectively, Fig. 3b) compare well with the dense-grid GGS method (i.e., 32 t km^{-2} d^{-1} and 21 t km^{-2} d^{-1}, respectively, Fig. 5). For the surveyed area (94–103 km^2) we obtain a total CO_2 flux of 283–409 t d^{-1} and for our scale-up we calculate a total flux of 757–901 t d^{-1} (over 340 km^2, the dashed yellow line excluding the eastern in Fig. 6a).

Our flux calculation identifies BBTM as the largest diffuse CO_2 emitter in the EARS. The flux is 2–4 × greater than Olkaria Volcanic Complex, Kenya (280 t d^{-1}; Cappelli et al., 2023), Abaya volcanic field (300 t d^{-1}; SMER, Hutchison et al., 2023) and Aluto (250–500 t d^{-1}; CMER, Hutchison et al., 2015). Higher CO_2 fluxes (~1100–4400 t d^{-1}; Fischer et al., 2019) are only known at Nyiragongo and Nyamuragira, two persistently active alkali-rich volcanoes located in the western branch of the EARS. These volcanoes are very different from most EARS volcanoes which are typified by silicic stratovolcanoes and calderas akin to BBTM. The high C emissions from BBTM most logically reflect its

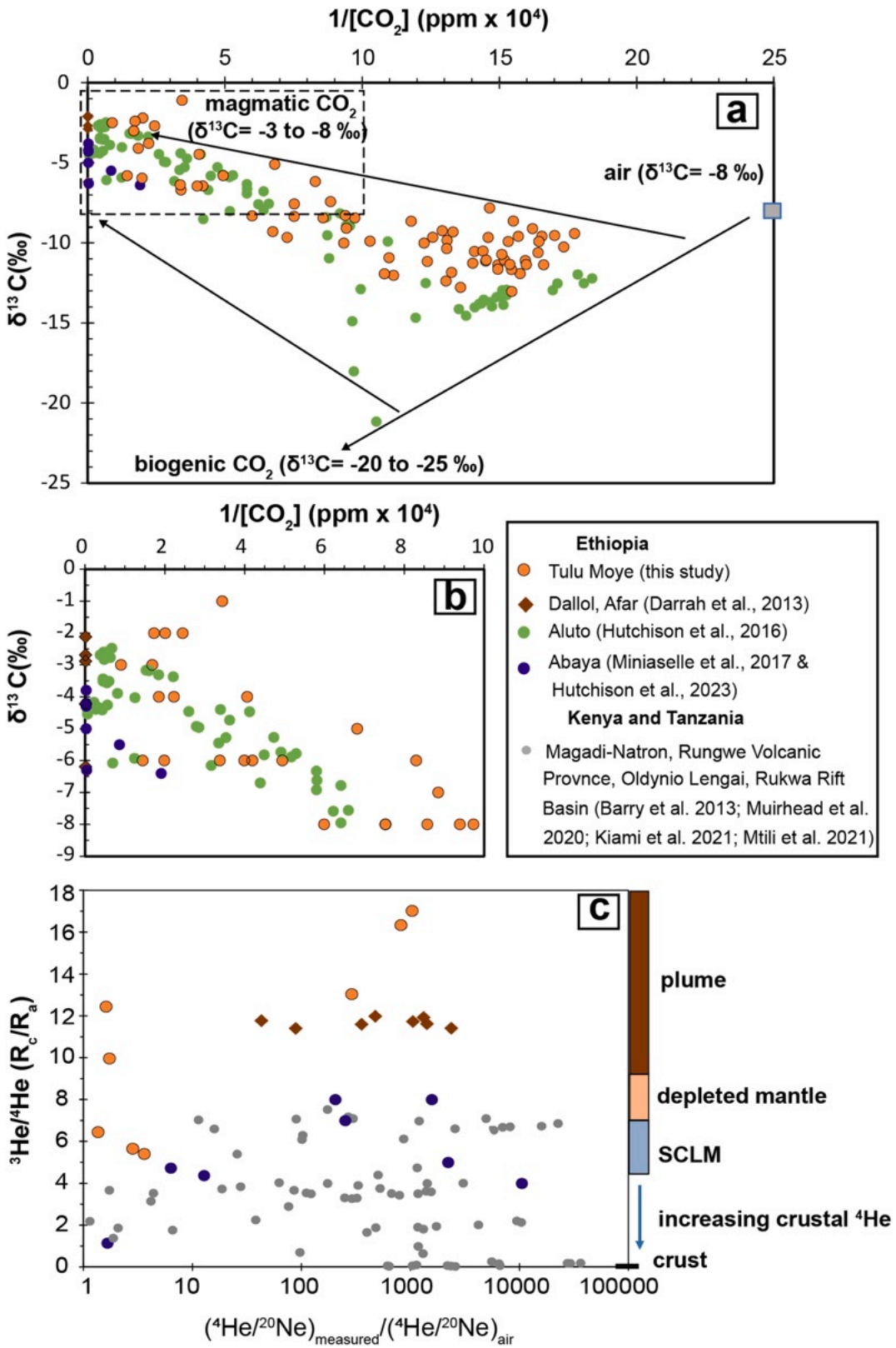

Fig. 7. a) Carbon isotopic composition ($\delta^{13}C$) of soil gas and fumarole samples from Ethiopia. $\delta^{13}C$ of CO_2 is plotted against the reciprocal of CO_2 concentration in the gas samples. The data are defined by three end members: air ($\delta^{13}C = -8$ ‰), biogenic ($\delta^{13}C = -20$ ‰ to -25 ‰) and magmatic C ($\delta^{13}C = -3$ to -8 ‰). b) inset of (a) showing the $\delta^{13}C$ values for the highest concentration samples. c) He isotopes versus *X*-value of fumarole and gas samples. The *X*-value is calculated as $(^4He/^{20}Ne)_{measured}/(^4He/^{20}Ne)_{air}$. $^3He/^4He$ is corrected for air and given in R_c/R_a notation. The coloured bars on the right represents the $^3He/^4He$ for depleted mid-ocean ridge basalts (MORB), subcontinental lithospheric mantle (SLCM), plume and crust endmembers after values from Gibson et al. (2024), Hutchison et al. (2023), Gilfillan et al. (2019) Hilton et al. (2011) and Graham (2002). The gray colored samples are taken from Magadi-Natron, Rungwe Volcanic Province, Oldynio Lengai, Rukwa Rift Basin after Barry et al. (2013), Muirhead et al. (2020), Kiami et al. (2021) and Mtili et al. (2021).

large melt-rich magmatic system, supported by magnetotelluric images that reveal a 1–10 km^3 upper crustal melt body with inferred melt fractions of 20–30 vol. % (Samrock et al., 2021). These inferred melt fractions are greater than other MER systems (i.e. Aluto, 10–15 vol. %, Dambly et al., 2023) and indicate a more extensive transcrustal magmatic system at BBTM (Samrock et al., 2021) consistent with the greater volatile flux.

Current estimates of C emissions from the Ethiopian Rift (Hunt et al., 2017) are based on CO_2 flux measurements from Aluto. As outlined above, Aluto has significantly lower melt fractions than BBTM but also other volcanoes such as Corbetti (also located in the CMER, Dambly et al., 2024). It follows that the CO_2 flux from Aluto (250–500 t d^{-1}) is not representative of all systems and that a re-appraisal of rift-scale CO_2 flux is required. Since our new CO_2 measurements are focused on degassing associated with large volcanic edifices, we calculate the on-edifice degassing along the different sectors of the Ethiopian Rift. We estimate the number of diffusely degassing volcanoes using the Global Volcanism Program database (Global Volcanism Program, 2024) and include only those that consistently exhibit thermal manifestations (Supplementary Table S4). We take the CO_2 flux from Aluto (Hutchison et al., 2015) and BBTM (this study) as lower and upper limits, respectively. In defining the different sectors of the MER, we follow the classification of Hayward and Ebinger (1996) and Corti (2009). No formal definition exists for the NMER-Afar boundary, and so we delineate three regions based on the presence or absence of seismic anomalies for mantle melting: NMER, southern Afar and central Afar (detailed in Section 5.3).

Our calculation (Fig. 8b, Supplementary Table S4) shows that the volcanic CO_2 flux is lowest in the SMER (90–330 kt yr^{-1}), and high in the CMER (450–1650 kt yr^{-1}), NMER (630–2310 kt yr^{-1}), and central Afar (450–1650 kt yr^{-1}). Our definition of central Afar includes only 5 volcanoes, but if we include all volcanic systems of Afar (up to Northern Afar and Dallol) the total flux for the region is 1260–4620 kt yr^{-1}. Summing all contributions from the Ethiopian Rift then the total CO_2 flux from the volcanic edifices is 2500–9200 kt yr^{-1}. The EARS comprises ~70 volcanoes exhibiting hydrothermal manifestations (Cappelli et al., 2023) and so using the lower and upper volcanic CO_2 flux limits from Ethiopia we estimate total emissions from the EARS to be 6300–23,100 kt yr^{-1}. This is at the low end of the Lee et al. (2016) estimate but still represents 7–24 % of all mid ocean ridge degassing (Marty and Tolstikhin, 1998). It is important to note that our estimate does not account for off-edifice degassing via fault-controlled fumaroles and hot springs. Flux estimates for these are very poorly constrained at present and based on Hunt et al. (2017) they may represent between 15 and 250 % of the volcanic edifice emissions.

Our CO_2 emission estimates are directly tied to the numbers of volcanic edifices in each rift sector, and the large number of edifices in CMER, NMER and central Afar suggest greater volumes of magmatic intrusion in these sectors. An additional test for this hypothesis is to measure the number of discrete volcanic vents (Fig. 8c), including mafic fissure vents and scoria cones distal to silicic volcanoes, which serve as a proxy for magma flux. We find that changes in vent density match the changing number of large volcanic edifices and support the notion that magma flux is enhanced in the high CO_2 flux rift sectors. Although individual vents are monogenic and do not necessarily contribute to CO_2 flux today, these data support along-rift changes in surface volcanism and magma flux which we see replicated in the volcanic CO_2 emissions (Fig. 8).

5.3. Changing volatile emissions and sources along the Ethiopian Rift

Having established that there is likely to be significant along-rift

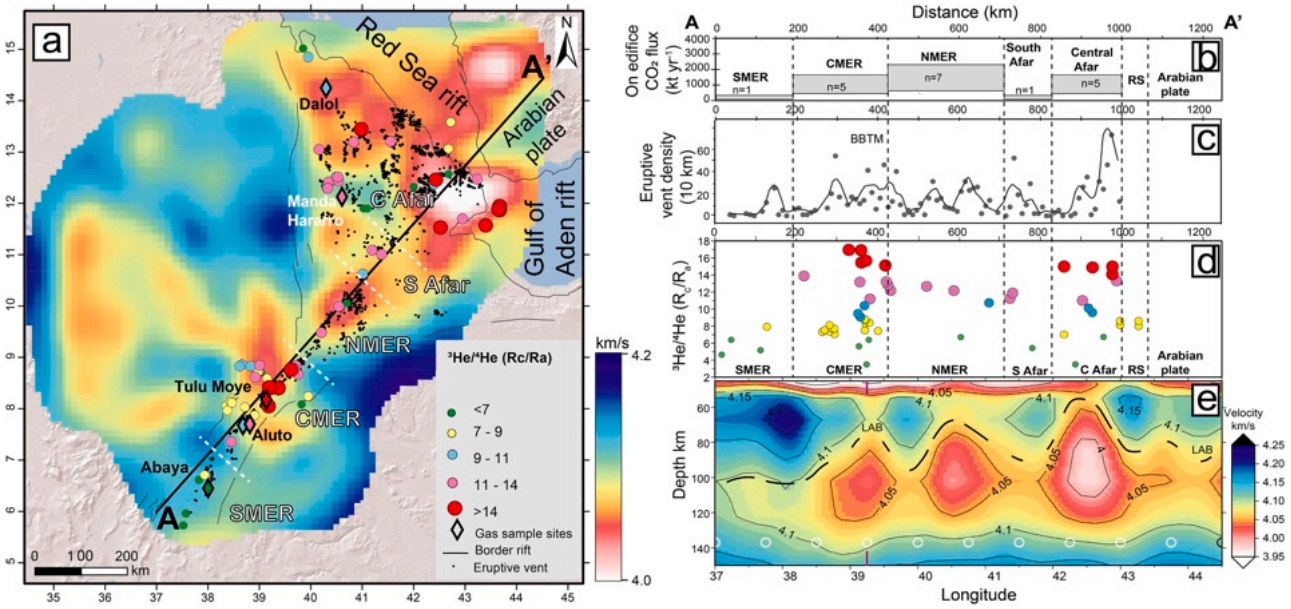

Fig. 8. (a) Map showing shear wave velocities across the Ethiopian Rift (after Chambers et al., 2022) overlain with $^3He/^4He$ from fumaroles and rocks. The average depth slice of shear wave velocity is between 40 and 130 km depth (results from and individual depth slices can be viewed in Chambers et al., 2022). Red and pink colours show slower velocities, and blue faster velocities. Shear velocities <4.05 km s^{-1} are interpreted as zones of partial melt. Our compilation of $^3He/^4He$ and references are given in full in Supplementary Table S5; diamonds show fumarole samples, and circles show rock samples (from mafic minerals and glasses) and the rock samples represent the samples of the rift floor <2 Ma age. The dashed while lines represent the boundary between the rift sectors and a transect line is labelled A-A'. b) CO_2 emissions in the different sectors of the rift (calculated using our new CO_2 fluxes and the number of large volcanic edifices with thermal activity, given by n). c) c) volcanic vent density per 10 km along the Ethiopian Rift (A-A'), which includes all vents (mafic and silicic) identifiable by remote sensing. The black line shows the smoothed average vent density values along the profile. BBTM stands for Bora-Baricha-Tulu Moye. d) $^3He/^4He$ along the A-A' profile line. e) cross-section of shear wave velocity at 40–150 km depth, from Chambers et al. 2022. This corresponds to the same profile line A-A'. The highest $^3He/^4He$ values correlate with the slower velocity anomalies (i.e. regions high mantle melt production) indicated by the red and pink colours in CMER and Afar. It is important to note that while crustal thickness decrease from CMER to Afar (from ~40 to 20 km, Lewi, 2024), we interpret the lithosphere-asthenosphere boundary to be shallow in the zones of overlying these melt zones in the CMER, NMER and central Afar.

variation in CO_2 emissions we now consider whether flux variations are linked to changing source contributions (e.g. plume, SCLM or crust) or variations in rifting processes (i.e. melt production and lithospheric thinning). Helium isotopes are a powerful tracer of volatile sources (Fig. 7c) and allow us to evaluate spatial variations along and across the rift. The lowest fumarole $^3He/^4He$ values are in the SMER (4.1–7.5 R_a, Minissale et al., 2017; Hutchison et al., 2023), while the highest are present in Afar (8–13 Ra, Marty et al., 1996; Darrah et al., 2013) and the CMER at BBTM (10–17 R_a, this study, Ruggieri and Magro, 1999 and Scarsi and Craig, 1996) (Fig. 8a).

$^3He/^4He$ analyses of fumarole gases in Ethiopia are limited (Fig. 8) and to obtain more detailed insights into the spatial variation of He isotopes we compiled existing measurements of $^3He/^4He$ in minerals (mainly pyroxene and olivine) from volcanic rocks and mantle xenoliths (Supplementary Table S5). These samples (Fig. 8a) have high $^3He/^4He$ (up to ~17 R_a) in the CMER, NMER and Afar and lower values (up to ~5 R_a) in the SMER (Marty et al., 1996; Scarsi and Craig, 1996; Rooney et al., 2012b). The highest $^3He/^4He$ of fumarole gases are consistent with the values in local volcanic rocks (both at BBTM and elsewhere). This confirms that the least air-contaminated fumarole gases provide good constraints on mantle source $^3He/^4He$ (Barry et al., 2013; Halldórsson et al., 2014). It is also clear that the strongest deep mantle He isotope values are present in the CMER.

Large-scale geophysical datasets provide insights into sub-rift architecture and mantle melting. Fig. 8a shows a map of shear wave velocity in the crust and upper mantle (i.e., an average of the 40–130 km depth, averaging the lithospheric mantle and top of the asthenosphere for visualisation purposes). Fig. 8e shows a depth cross-section along the MER and Afar (A-A'). Mantle velocities are primarily affected by temperature (Chambers et al., 2022) and as Ethiopian mantle temperatures are elevated (Rooney et al., 2012a) this will decrease the measured shear wave velocity. By accounting for temperature using a Burgers model, Chambers et al. (2022) found velocities <4.05 km s^{-1} require a fluid component which, given the ongoing volcanism in Ethiopia, is interpreted as partial melt within the asthenosphere. Three regions of anomalously slow shear wave velocity (Vs <4.05 km s^{-1}) are observed in the CMER, NMER and central Afar. These anomalies are ~100–200 km wide and spaced ~100–300 km apart (Fig. 8e) and compare with melt anomalies observed beneath oceanic spreading centres (e.g. the Gulf of California, Wang et al. 2009). Note that as no formal definition of the NMER-Afar boundary exists, we use these shear wave velocity anomalies to delineate the northern extent of the NMER, as well as southern Afar and central Afar.

A key feature of the shear wave velocity models is that the depth to the top of the partial melt zones varies. The CMER melt zone is limited to a depth of 90 km while in Afar the top of the melt is at 60 km (Fig. 8e). These depths are broadly consistent with that of melt production modelled from geochemical data (Ferguson et al., 2013), supporting the interpretation of them being zones of asthenospheric melt production below the plate. The depth to the top of the melt zone is similar to the depth to the lithosphere asthenosphere boundary (Lavayssière et al., 2019; Chambers et al., 2022), with shallowing of the top of the melt zone into Afar (consistent with lithospheric thinning, Keir et al., 2015).

Directly comparing He isotope values with shear wave velocity models (Fig. 8a) reveals a reasonable correspondence (Fig. 8d). High $^3He/^4He$ values (>10 R_a) extend across the CMER and Central Afar, and overly a broad region of slow velocity anomalies. Importantly, the highest $^3He/^4He$ (>14 R_a) are found in the CMER and Afar and correspond with inferred zones of partial melting (Fig. 8e). No slow velocity anomalies are observed in the SMER (i.e. Vs >4.05 km s^{-1}) and this corresponds to low $^3He/^4He$ (4–8 R_a, Fig. 8e), suggesting less mantle derived helium and proportionally more helium from radiogenic-rich sources. The NMER (Fig. 8e) is characterized by a slower and larger velocity anomaly than the CMER, which may indicate greater magma production, but there are no values >14 R_a. Given the limited He isotope measurements in the NMER it is unclear whether the lack of correlation between slow shear wave velocity and high $^3He/^4He$ is real or simply reflects a lack of measurements. Nevertheless, the comparison between the geophysical and geochemical indicators reveals a broad region of plume-influenced melting with elevated $^3He/^4He$ (>11 R_a) extending from the CMER into Afar and the Gulf of Aden and, in addition, segmented partial melt zones along the rift that spatially correlate with high $^3He/^4He$ plume-like compositions.

Another insight is that in regions of deeper melting (i.e. the CMER), the $^3He/^4He$ is characterized by the highest values observed along the EARS (12–17 R_a, Fig. 8d). In Afar, where partial melts are inferred at both deep and shallow levels, up to 60 km, $^3He/^4He$ values are slightly lower (11–15 R_a); though still clearly influenced by upwelling deep mantle. Geochemical analyses of rift basalts suggest that the upper mantle beneath Afar and the MER comprises a hybrid mixture of depleted ambient upper mantle and Pan-African continental lithosphere (Scarsi and Craig, 1996; Rooney et al., 2012b). Melting of continental lithosphere will introduce $^3He/^4He$ of ≤8 R_a (Gibson et al., 2024), and thus, the greater component of hybrid upper mantle in Afar can explain the somewhat lower $^3He/^4He$ values there relative to the CMER. This suggests that mantle beneath Ethiopia does have vertical variations in $^3He/^4He$, with the highest plume-like values associated with deeper mantle melting (>100 km).

In Section 5.2 we showed that there is clear along-rift variation in the number of discrete volcanic vents and larger volcanic edifices, and that we predict significant variation in CO_2 flux between the different rift sectors (Fig. 8b). A key question is whether the CO_2 flux is more strongly influenced by melting lithologies (i.e., the ratios of asthenospheric: lithospheric:plume mantle and overprinting crustal materials) or by rates of mantle melt production. Helium isotopes are a good proxy for volatile sources, and our data compilation shows that while lithospheric sources dominate in southern Ethiopia (Fig. 8d) and may be an important store of mantle C (Foley and Fischer, 2017), volcanic CO_2 emissions are relatively low. The highest CO_2 emissions are associated with regions of intense mantle melting and lithospheric thinning, i.e. the CMER, NMER and central Afar, which is evidenced by their low velocity seismic anomalies (Fig. 8e, Gallacher et al., 2016; Chambers et al., 2022). In regions of high mantle melt production, magma fluxes into the crust are higher, there is a greater number of volcanic vents at the surface (Fig. 8c), and this likely accounts for the higher CO_2 degassing. Therefore, the primary control on deep C emissions in a mature continental rift like Ethiopia is the rate of mantle melt production caused by lithospheric thinning.

A final important point is that rift sectors that exhibit enhanced partial melting and degassing also display a stronger deep mantle $^3He/^4He$ value (Fig. 8). We hypothesise that within sectors of more extensive and deeper melting, magma fluxes to the crust are higher and hence the plume-derived $^3He/^4He$ is less susceptible to overprinting by lithospheric mantle and crustal sources. This is consistent with large-scale deep mantle contributions across the sub-EARS mantle (c.f. Halldórsson et al., 2014; Chen et al., 2025; Watts et al., 2025), but with the important caveat that spatially variable mantle melting and lithospheric overprint strongly influences the preservation of the $^3He/^4He$ signal.

6. Conclusions

An investigation of CO_2 flux and He and C isotopes at one of Ethiopia's largest volcanic systems (Bora-Baricha-Tulu Moye, BBTM) provides valuable insights into structural controls on degassing, magnitude of C emissions and volatile sources. The main findings are:

1. Volcanic and tectonic structures control degassing. Rift-aligned faults and major volcano-tectonic segments (i.e. the Salen range, Fig. 3) show elevated gas emissions, as do NW-SE rift transverse faults.

2. The total volcanic CO_2 gas emission from BBTM is 757–901 t d^{-1}, making it the largest diffuse C emitter currently known in the EARS (Fig. 8).
3. He isotopes from BBTM fumaroles show significant plume contributions (up to 17 R_a).
4. He isotopes reveal along-rift variations in volatile sources, with the highest $^3He/^4He$ values observed in the CMER.
5. We predict significant along-rift variations in C flux with the CMER, NMER and central Afar being the most significant degassing sectors (450–1650 kt yr^{-1} 630–2310 kt yr^{-1} and 450–1650 kt yr^{-1}), respectively. Total CO_2 flux from volcanic edifices across the Ethiopian Rift is 2500–9200 kt yr^{-1}.
6. High $^3He/^4He$ regions (>14 R_a) align with the segmented pattern of melt production and magmatic intrusion identified by uppermost mantle seismic imaging. Carbon emissions and plume contributions are particularly elevated in regions of greatest lithospheric thinning and mantle melting (i.e. the CMER and Afar).

Our data emphasise important along-strike variations in volatile emissions in Ethiopia which appear to be most strongly controlled by the rates of mantle melting. These observations contrast with less mature rift sectors, i.e. Tanzania, where the lithospheric mantle has yet to be extensively thinned, and where large lateral gradients in lithospheric thickness and composition explain spatial variations in mantle CO_2 flux (Muirhead et al. 2020). These studies highlight the need for more systematic and spatially resolved CO_2 flux and noble gas isotope data sets along and across the EARS to better understand how rifting unlocks deep mantle C, and the significance of these fluxes over geological times-scales (Brune et al. 2017).

CRediT authorship contribution statement

Abate A. Melaku: Writing – review & editing, Writing – original draft, Visualization, Validation, Methodology, Investigation, Formal analysis, Data curation, Conceptualization. **Gemechu B. Teferi:** Writing – review & editing, Investigation. **Takele Mihretie:** Writing – review & editing, Investigation. **Snorri Gudbrandsson:** Writing – review & editing, Resources, Conceptualization. **Yared Sinetebeb:** Writing – review & editing, Investigation. **Peter H. Barry:** Writing – review & editing, Methodology, Investigation. **Tobias P. Fischer:** Methodology, Investigation. **Finlay M. Stuart:** Writing – review & editing, Validation, Supervision, Resources, Methodology, Conceptualization. **Ugur Balci:** Writing – review & editing, Methodology. **Sæmundur A. Halldórsson:** Writing – review & editing, Methodology, Investigation. **Chris J. Ballentine:** Methodology. **Darren J. Hillegonds:** Methodology. **Emma L. Chambers:** Writing – review & editing, Visualization, Resources. **Derek Keir:** Writing – review & editing, Visualization, Resources. **Richard Bates:** Writing – review & editing, Supervision. **William Hutchison:** Writing – review & editing, Writing – original draft, Visualization, Validation, Supervision, Methodology, Investigation, Data curation, Conceptualization.

Declaration of competing interest

The authors declare that they have no known competing financial interests or personal relationships that could have appeared to influence the work reported in this paper.

Acknowledgments

This work was supported by Global Challenges Research Fund (GCRF) grant to University of St Andrews and Reykjavik Geothermal. W. Hutchison is funded by a UKRI Future Leaders Fellowship (MR/S033505/1). P. Barry acknowledges NSF award 2319897. We thank Addis Ababa University for providing a vehicle for fieldwork, as well as A. Teka and Tulu Moye Geothermal staff for their invaluable support during fieldwork. We acknowledge the assistance of the local and regional government officials and the local community for granting permission and facilitating the fieldwork. We thank Fuad and Abdi for their help in the field and for facilitating communication with the local people.

The manuscript greatly benefited from four anonymous reviews. We would like to thank the reviewers for their pertinent and constructive comments, and Chiara Petrone for editorial handling.

Supplementary materials

Supplementary material associated with this article can be found, in the online version, at doi:10.1016/j.epsl.2025.119782.

Data availability

Data will be made available on request.

References

Acocella, V., Korme, T., Salvini, F.S., 2003. Formation of normal faults along the axial zone of the Ethiopian Rift. www.elsevier.com/locate/jstrugeo.

Agostini, A., Bonini, M., Corti, G., Sani, F., Mazzarini, F., 2011. Fault architecture in the Main Ethiopian Rift and comparison with experimental models: implications for rift evolution and Nubia-Somalia kinematics. Earth Planet. Sci. Lett 301 (3–4), 479–492. https://doi.org/10.1016/j.epsl.2010.11.024.

Balci, U., Stuart, F.M., Barrat, J.A., Grima, A.G., van der Zwan, F.M., 2024. The origin and implications of primordial helium depletion in the Afar mantle plume. Commun. Earth Environ. 5 (1). https://doi.org/10.1038/s43247-024-01675-2.

Barry, P.H., De Moor, J.M., Chiodi, A., Aguilera, F., Hudak, M.R., Bekaert, D.V., Turner, S.J., Curtice, J., Seltzer, A.M., Jessen, G.L., Osses, E., Blamey, J.M., Amenábar, M.J., Selci, M., Cascone, M., Bastianoni, A., Nakagawa, M., Filipovich, R., Bustos, E., Giovannelli, D., 2022. The helium and carbon isotope characteristics of the Andean convergent margin. Front. Earth Sci. 10. https://doi.org/10.3389/feart.2022.897267.

Barry, P.H., Hilton, D.R., Fischer, T.P., de Moor, J.M., Mangasini, F., Ramirez, C., 2013. Helium and carbon isotope systematics of cold 'mazuku' CO2 vents and hydrothermal gases and fluids from Rungwe Volcanic Province, southern Tanzania. Chem. Geol. 339, 141–156. https://doi.org/10.1016/j.chemgeo.2012.07.003.

Benvenuti, M., Corti, G., Keir, D., Sani, F., 2023. Transverse tectonics control on the late quaternary development of the Central Main Ethiopian Rift. Ital. J. Geosci. 142 (1), 42–56. https://doi.org/10.3301/IJG.2023.05.

Boccaletti, M., Bonini, M., Mazzuoli, R., Abebe, B., Piccardi, L., Tortorici, L., 1998. Quatemary oblique extensional tectonics in the Ethiopian Rift (Horn of Africa). Tectonophysics 287.

Boyce, A., Kounoudis, R., Bastow, I.D., Cottaar, S., Ebinger, C.J., Ogden, C.S., 2023. Mantle wavespeed and discontinuity structure below East Africa: implications for cenozoic hotspot tectonism and the development of the Turkana Depression. Geochem. Geophys. Geosystems 24 (8). https://doi.org/10.1029/2022GC010775.

Brune, S., Williams, S.E., Müller, R.D., 2017. Potential links between continental rifting, CO2 degassing and climate change through time. Nat. Geosci. 10 (12), 941–946. https://doi.org/10.1038/s41561-017-0003-6.

Cappelli, L., Wallace, P.A., Randazzo, A., Kamau, P.M., Njoroge, R.W., Otieno, V., Tubula, M.S., Mariita, N.O., Mangi, P., Fontijn, K., 2023. Diffuse soil CO_2 emissions at rift volcanoes: structural controls and total budget of the Olkaria Volcanic Complex (Kenya) case study. J. Volcanol. Geotherm. Res. 443. https://doi.org/10.1016/j.jvolgeores.2023.107929.

Cardellini, C., Chiodini, G., Frondini, F., 2003. Application of stochastic simulation to CO_2 flux from soil: mapping and quantification of gas release. J. Geophys. Res.: Solid Earth. 108 (B9). https://doi.org/10.1029/2002jb002165.

Chambers, E.L., Harmon, N., Rychert, C.A., Gallacher, R.J., Keir, D., 2022. Imaging the seismic velocity structure of the crust and upper mantle in the northern East African Rift using Rayleigh wave tomography. Geophys. J. Int. 230 (3), 2036–2055. https://doi.org/10.1093/gji/ggac156.

Chang, S.J., Kendall, E., Davaille, A., Ferreira, A.M.G., 2020. The evolution of mantle plumes in East Africa. J. Geophys. Res.: Solid Earth. 125 (12). https://doi.org/10.1029/2020JB019929.

Chen, B., Györe, D., Mutia, T., Stuart, F.M., 2025. Neon isotopes in geothermal gases from the Kenya rift reveal a common deep mantle source beneath East Africa. Geophys Res. Lett. 52 (10). https://doi.org/10.1029/2025GL115169.

Chiodini, G., Caliro, S., Cardellini, C., Avino, R., Granieri, D., Schmidt, A., 2008. Carbon isotopic composition of soil CO_2 efflux, a powerful method to discriminate different sources feeding soil CO2 degassing in volcanic-hydrothermal areas. Earth Planet, Sci., Lett. 274 (3–4), 372–379. https://doi.org/10.1016/j.epsl.2008.07.051.

Corti, G., Molin, P., Sembroni, A., Bastow, I.D., Keir, D., 2018. Control of pre-rift lithospheric structure on the architecture and evolution of continental rifts: insights from the main Ethiopian rift. East Afr., Tecton. 37 (2), 477–496. https://doi.org/10.1002/2017TC004799.

Corti, G., 2009. Continental rift evolution: from rift initiation to incipient break-up in the Main Ethiopian Rift, East Africa. Earth-Sci. Rev. 96 (1–2), 1–53. https://doi.org/10.1016/j.earscirev.2009.06.005.

Dambly, M.L.T., Samrock, F., Grayver, A., Eysteinsson, H., Saar, M.O., 2024. Geophysical imaging of the active magmatic intrusion and g eothermal reser voir formation beneath the Corbetti prospect, Main Ethiopian Rift. Geophys. J. Int. 236 (3), 1764–1781. https://doi.org/10.1093/gji/ggad493.

Dambly, M.L.T., Samrock, F., Grayver, A.V., Saar, M.O., 2023. Insights on the interplay of rifting, transcrustal magmatism and formation of geothermal resources in the Central segment of the Ethiopian Rift revealed by 3-D magnetotelluric imaging. J. Geophys. Res.: Solid Earth 128 (7). https://doi.org/10.1029/2022JB025849.

Darrah, T.H., Tedesco, D., Tassi, F., Vaselli, O., Cuoco, E., Poreda, R.J., 2013. Gas chemistry of the Dallol region of the Danakil Depression in the Afar region of the northern-most East African Rift. Chem., Geol. 339, 16–29. https://doi.org/10.1016/j.chemgeo.2012.10.036.

Ebinger, C., 2005. Continental break-up: the East African perspective. Astron. Geophys. 46 (2), 2.16–2.21. https://doi.org/10.1111/j.1468-4004.2005.46216.x.

Ferguson, D.J., MacLennan, J., Bastow, I.D., Pyle, D.M., Jones, S.M., Keir, D., Blundy, J. D., Plank, T., Yirgu, G., 2013. Melting during late-stage rifting in Afar is hot and deep. Nature 499 (7456), 70–73. https://doi.org/10.1038/nature12292.

Fischer, T.P., Arellano, S., Carn, S., Aiuppa, A., Galle, B., Allard, P., Lopez, T., Shinohara, H., Kelly, P., Werner, C., Cardellini, C., Chiodini, G., 2019. The emissions of CO2 and other volatiles from the world's subaerial volcanoes. Sci. Rep. 9 (1). https://doi.org/10.1038/s41598-019-54682-1.

Foley, S.F., Fischer, T.P., 2017. An essential role for continental rifts and lithosphere in the deep carbon cycle. Nature Geoscience 897–902. https://doi.org/10.1038/s41561-017-0002-7. Vol. 10, Issue 12.

Gallacher, R.J., Keir, D., Harmon, N., Stuart, G., Leroy, S., Hammond, J.O.S., Kendall, J. M., Ayele, A., Goitom, B., Ogubazghi, G., Ahmed, A., 2016. The initiation of segmented buoyancy-driven melting during continental breakup. Nat. Commun. 7. https://doi.org/10.1038/ncomms13110.

Gerlach, T.M., Taylor, B.E., 1990. Carbon isotope constraints on degassing of carbon dioxide from Kilauea Volcano. Geochim. Cosmochim. Acta 54 (7), 2051–2058. https://doi.org/10.1016/0016-7037(90)90270-U.

Gibson, S.A., Crosby, J.C., Day, J.A.F., Stuart, F.M., DiNicola, L., Riley, T.R., 2024. Systematic behaviour of 3He/4He in Earth's continental mantle. Geochim. Cosmochim. Acta 384, 44–64. https://doi.org/10.1016/j.gca.2024.09.009.

Gilfillan, S.M.V., Györe, D., Flude, S., Johnson, G., Bond, C.E., Hicks, N., Lister, R., Jones, D.G., Kremer, Y., Haszeldine, R.S., Stuart, F.M., 2019. Noble gases confirm plume-related mantle degassing beneath Southern Africa. Nat. Commun. 10 (1). https://doi.org/10.1038/s41467-019-12944-6.

Global Volcanism Program, 2024. [Database] Volcanoes of the World (v. 5.2.7; 21 Feb 2025). Distributed by Smithsonian Institution, compiled by Venzke, E. https://doi.org/10.5479/si.GVP.VOTW5-2024.5.2.

Graham, D.W., 2002. Noble gas isotope geochemistry of mid-ocean ridge and ocean island basalts: characterization of mantle source reservoirs. Rev. Mineral. Geochem. 47. https://doi.org/10.2138/rmg.2002.47.8.

Greenfield, T., Keir, D., Kendall, J.M., Ayele, A., 2019a. Low-frequency earthquakes beneath Tullu Moye volcano, Ethiopia, reveal fluid pulses from shallow magma chamber. Earth Planet., Sci., Lett. 526. https://doi.org/10.1016/j.epsl.2019.115782.

Greenfield, T., Keir, D., Kendall, J.M., Ayele, A., 2019b. Seismicity of the Bora-Tullu Moye volcanic field, 2016–2017. Geochem. Geophys. Geosyst. 20 (2), 548–570. https://doi.org/10.1029/2018GC007648.

Györe, D., Stuart, F.M., Gilfillan, S.M.V., Waldron, S., 2015. Tracing injected CO_2 in the Cranfield enhanced oil recovery field (MS, USA) using He, Ne and Ar isotopes. Int. J. Greenh. Gas Control. 42, 554–561. https://doi.org/10.1016/j.ijggc.2015.09.009.#.

Halldórsson, S.A., Hilton, D.R., Marshall, E.W., Ranta, E., Ingvason, A., Chakraborty, S., Robin, J.G., Rasmussen, M.B., Gibson, S.A., Ono, S., Scarsi, P., Abebe, T., Hopp, J., Barry, P.H., Castillo, P.R., 2022. Evidence from gas-rich ultramafic xenoliths for Superplume-derived recycled volatiles in the East African sub-continental mantle. Chem., Geol. 589. https://doi.org/10.1016/j.chemgeo.2021.120682.

Halldõrsson, S.A., Hilton, D.R., Scarsi, P., Abebe, T., Hopp, J., 2014. A common mantle plume source beneath the entire East African Rift System revealed by coupled helium-neon systematics. Geophys. Res. Lett. 41 (7), 2304–2311. https://doi.org/10.1002/2014GL059424.

Halldórsson, S.A., Hilton, D.R., Troll, V.R., Fischer, T.P., 2013. Resolving volatile sources along the western Sunda arc, Indonesia. Chem, Geol 339, 263–282. https://doi.org/10.1016/j.chemgeo.2012.09.042.

Hayward, N.J., Ebinger, C.J., 1996. Soft plates and hot spots: views from Afar. J. Geophys. Res.: Solid Earth. 101 (B10), 21859–21876. https://doi.org/10.1029/96jb02118.

Hilton, D.R., Halldórsson, S.A., Barry, P.H., Fischer, T.P., De Moor, J.M., Ramirez, C.J., Mangasini, F., Scarsi, P., 2011. Helium isotopes at Rungwe Volcanic Province, Tanzania, and the origin of East African Plateaux. Geophys. Res. Lett. 38 (21). https://doi.org/10.1029/2011GL049589.

Hilton, D.R., 1996. The helium and carbon isotope systematics of a continental geothermal system: results from monitoring studies at Long Valley caldera (California, U.S.A.). Chem., Geol. 127.

Hunt, J.A., Zafu, A., Mather, T.A., Pyle, D.M., Barry, P.H., 2017. Spatially variable CO_2 degassing in the Main Ethiopian Rift: implications for magma storage, volatile transport, and Rift-related emissions. Geochem. Geophys. Geosystems 18 (10), 3714–3737. https://doi.org/10.1002/2017GC006975.

Hutchison, W., Ogilvie, E.R.D., Birhane, Y.G., Barry, P.H., Fischer, T.P., Ballentine, C.J., Hillegonds, D.J., Biggs, J., Albino, F., Cervantes, C., Guðbrandsson, S., 2023. Gas emissions and subsurface architecture of fault-controlled geothermal systems: a case study of the North Abaya geothermal area. Geochem. Geophys. Geosyst. 24 (4). https://doi.org/10.1029/2022GC010822.

Hutchison, W., Biggs, J., Mather, T.A., Pyle, D.M., Lewi, E., Yirgu, G., Caliro, S., Chiodini, G., Clor, L.E., Fischer, T.P., 2016. Causes of unrest at silicic calderas in the East African Rift: new constraints from InSAR and soil-gas chemistry at Aluto volcano, Ethiopia. Geochem. Geophys. Geosyst. 17 (8), 3008–3030. https://doi.org/10.1002/2016GC006395.

Hutchison, W., Mather, T.A., Pyle, D.M., Biggs, J., Yirgu, G., 2015. Structural controls on fluid pathways in an active rift system: a case study of the Aluto volcanic complex. Geosphere 11 (3), 542–562. https://doi.org/10.1130/GES01119.1.

Keir, D., Bastow, I.D., Corti, G., Mazzarini, F., Rooney, T.O., 2015. The origin of along-rift variations in faulting and magmatism in the Ethiopian Rift. Tectonics 34 (3), 464–477. https://doi.org/10.1002/2014TC003698.

Keir, D., Ebinger, C.J., Stuart, G.W., Daly, E., Ayele, A., 2006. Strain accommodation by magmatism and faulting as rifting proceeds to breakup: seismicity of the northern Ethiopian rift. J. Geophys. Res.: Solid Earth 111 (5). https://doi.org/10.1029/2005JB003748.

Kimani, C.N., Kasanzu, C.H., Tyne, R.L., Mtili, K.M., Byrne, D.J., Kazimoto, E.O., Hillegonds, D.J., Ballentine, C.J., Barry, P.H., 2021. He, Ne, Ar and CO2 systematics of the Rungwe Volcanic Province, Tanzania: implications for fluid source and dynamics. Chem., Geol. 586. https://doi.org/10.1016/j.chemgeo.2021.120584.

Korme, T., Acocella, V., Bekele, Abebel, 2004. The role of pre-existing structures in the origin, propagation and architecture of faults in the Main Ethiopian Rift. Int. Assoc. Gondwana Res. 7 (2).

Lavayssière, A., Greenfield, T., Keir, D., Ayele, A., Kendall, J.M., 2019. Local seismicity near the actively deforming Corbetti volcano in the Main Ethiopian Rift. J. Volcanol. Geotherm. Res. 381, 227–237. https://doi.org/10.1016/j.jvolgeores.2019.06.008.

Lee, H., Muirhead, J.D., Fischer, T.P., Ebinger, C.J., Kattenhorn, S.A., Sharp, Z.D., Kianji, G., 2016. Massive and prolonged deep carbon emissions associated with continental rifting. Nat. Geosci. 9 (2), 145–149. https://doi.org/10.1038/ngeo2622.

Lewi, E., 2024. Seamless map of depth to the Moho Interface in the Afro-Arabian region using gravity data derived from EGM2008. Geochem. Geophys. Geosyst. 25 (7). https://doi.org/10.1029/2023GC011322.

Marty, B., Appora, I., Barrat, J.A., Deniel, C., Vellutini, P., Vidal, P., 1993. He, Ar, Sr, Nd and Pb isotopes in volcanic rocks from Afar: evidence for a primitive mantle component and constraints on magmatic sources. Geochem. J. 27, 219–228.

Marty, B., Pik, R., Gezahegn, Y., 1996. Helium isotopic variations in Ethiopian plume lavas: nature of magmatic sources and limit on lower mantle contribution. Earth. Planet., Sci., Lett. 144.

Marty, B., Tolstikhin, I.N., 1998. CO_2 fluxes from mid-ocean ridges, arcs and plumes. Chem., Geol. 145 (3–4), 233–248. https://doi.org/10.1016/S0009-2541(97)00145-9.

Mtili, K.M., Byrne, D.J., Tyne, R.L., Kazimoto, E.O., Kimani, C.N., Kasanzu, C.H., Hillegonds, D.J., Ballentine, C.J., Barry, P.H., 2021. The origin of high helium concentrations in the gas fields of southwestern Tanzania. Chem., Geol. 585. https://doi.org/10.1016/j.chemgeo.2021.120542.

Minissale, A., Corti, G., Tassi, F., Darrah, T.H., Vaselli, O., Montanari, D., Montegrossi, G., Yirgu, G., Selmo, E., Teclu, A., 2017. Geothermal potential and origin of natural thermal fluids in the northern Lake Abaya area, Main Ethiopian Rift, East Africa. J. Volcanol. Geotherm. Res. 336, 1–18. https://doi.org/10.1016/j.jvolgeores.2017.01.012.

Muirhead, J.D., Fischer, T.P., Oliva, S.J., Laizer, A., van Wijk, J., Currie, C.A., Lee, H., Judd, E.J., Kazimoto, E., Sano, Y., Takahata, N., Tiberi, C., Foley, S.F., Dufek, J., Reiss, M.C., Ebinger, C.J., 2020. Displaced cratonic mantle concentrates deep carbon during continental rifting. Nature 582 (7810), 67–72. https://doi.org/10.1038/s41586-020-2328-3.

Pik, R., Marty, B., Hilton, D.R., 2006. How many mantle plumes in Africa? The geochemical point of view. Chem., Geol. 226, 100–114. https://doi.org/10.1016/j.chemgeo.2005.09.016.

Ritsema, J., Heijst, H.J.V., Woodhouse, J.H., 1999. Complex shear wave velocity structure imaged beneath Africa and Iceland. Science 286, 3. www.sciencemag.org.

Rooney, T.O., Herzberg, C., Bastow, I.D., 2012a. Elevated mantle temperature beneath East Africa. Geology 40, 27–30. https://doi.org/10.1130/g32382.1.

Rooney, T.O., Hanan, B.B., Graham, D.W., Furman, T., Blichert-toft, J., Schilling, J.G., 2012b. Upper mantle pollution during Afar plume-continental rift interaction. J. Petrol. 53 (2), 365–389. https://doi.org/10.1093/petrology/egr065.

Ruggieri, G., Magro, G., 1999. Helium isotopic composition of fluid inclusions from two Ethiopian geothermal fields. Geochem. Earth's Surf. Retrieved from. https://www.researchgate.net/publication/242215240.

Samrock, F., Grayver, A.V., Bachmann, O., Karakas, Ö., Saar, M.O., 2021. Integrated magnetotelluric and petrological analysis of felsic magma reservoirs: insights from Ethiopian rift volcanoes. Earth Planet, Sci., Lett. 559. https://doi.org/10.1016/j.epsl.2021.116765.

Samrock, F., Grayver, A.V., Eysteinsson, H., Saar, M.O., 2018. Magnetotelluric image of transcrustal magmatic system beneath the Tulu Moye geothermal prospect in the ethiopian Rift. Geophys Res. Lett. 45 (23). https://doi.org/10.1029/2018GL080333, 12,847-12,855.

Sawyer, G.M., Carn, S.A., Tsanev, V.I., Oppenheimer, C., Burton, M., 2008. Investigation into magma degassing at Nyiragongo volcano, Democratic Republic of Congo. Geochem. Geophys. Geosyst. 9 (2). https://doi.org/10.1029/2007GC001829.

Scarsi, P., Craig, H., 1996. Helium isotope ratios in Ethiopian Rift basalts. Earth. Planet., Sci., Lett. 144, 505–516.

Siegburg, M., Bull, J.M., Nixon, C.W., Keir, D., Gernon, T.M., Corti, G., Abebe, B., Sanderson, D.J., Ayele, A., 2020. Quantitative constraints on faulting and fault slip rates in the Northern Main Ethiopian Rift. Tectonics 39 (8). https://doi.org/10.1029/2019TC006046.

Tadesse, A.Z., Bedassa, G., Kervyn, M., Muluneh, A.A., Gudbrandsson, S., Yirgu, G., Ayalew, D., Fontijn, K., 2023a. Structural controls on magma pathways in the Bora-Baricha-Tullu Moye volcanic system, Main Ethiopian Rift. Volcanica 6 (2), 367–390. https://doi.org/10.30909/vol.06.02.367390.

Tadesse, A.Z., Fontijn, K., Caricchi, L., Bégué, F., Gudbrandsson, S., Smith, V.C., Gopon, P., Debaille, V., Laha, P., Terryn, H., Yirgu, G., Ayalew, D., 2023b. Pre-eruptive storage conditions and magmatic evolution of the Bora-Baricha-Tullu Moye volcanic system, Main Ethiopian Rift. Lithos 442–443. https://doi.org/10.1016/j.lithos.2023.107088.

Tadesse, A.Z., Fontijn, K., Melaku, A.A., Gebru, E.F., Smith, V.C., Tomlinson, E., Barfod, D., Gopon, P., Bégué, F., Caricchi, L., Laha, P., Terryn, H., Gudbrandsson, S., Yirgu, G., Ayalew, D., 2022. Eruption frequency and magnitude in a geothermally active continental rift: the Bora-Baricha-Tullu Moye volcanic complex, Main Ethiopian Rift. J. Volcanol. Geotherm. Res. 423. https://doi.org/10.1016/j.jvolgeores.2022.107471.

Wang, Y., Forsyth, D.W., Savage, B., 2009. Convective upwelling in the mantle beneath the Gulf of California. Nature 462 (7272), 499–501. https://doi.org/10.1038/nature08552.

Watts, E.J., Rees, R., Jonathan, P., Keir, D., Taylor, R.N., Siegburg, M., Chambers, E.L., Pagli, C., Cooper, M.J., Michalik, A., Milton, J.A., Hincks, T.K., Gebru, E.F., Ayele, A., Abebe, B., Gernon, T.M., 2025. Mantle upwelling at Afar triple junction shaped by overriding plate dynamics. Nat. Geosci. 18 (7), 661–669. https://doi.org/10.1038/s41561-025-01717-0.